Laminate Wrinkling Scaling Laws for Ideal Composites

T.G. Gutowski, G. Dillon, S. Chey, H. Li.

Laboratory for Manufacturing and Productivity
Massachusetts Institute of Technology
Cambridge, MA 02139
U.S.A.

for Flow Processes in Composite Materials '94
University College Galway, Ireland
July 7-9, 1994

Abstract

For the double diaphragm forming process, laminate wrinkling is a major failure mode for both thermoplastic and thermoset composites. In this paper, we compare experimental observations on the wrinkling of aligned fiber thermoset composites with theoretical scaling laws based on ideal kinematics. Differences between the ideal predictions and actual results are explained in terms of deviations from ideal kinematics. Differences between thermoplastic and thermoset composites are discussed, and an empirical scaling law for the effect of part size on wrinkling is given.

1. Introduction

The majority of parts manufactured from advanced composites are made by a labor intensive hand lay-up process. A potentially more cost effective technique is diaphragm forming, where the geometry of a given part is achieved in a single forming step. In combination with automated tape lay-up and ply cutting techniques, this process could offer a significant reduction in part costs when compared with conventional techniques. In diaphragm forming, a laminated prepreg preform is placed between elastic diaphragms and a vacuum is drawn to

ensure that the diaphragms make effective contact with the composite. Deformation to the tool geometry is achieved by the application of vacuum from beneath the tool, or by pressure from above, or a combination of both. The process is shown schematically in Figure 1.

Although diaphragm forming techniques were first applied to thermoplastic matrix composites in the 1970's, recent efforts have been directed toward implementation of the process utilizing thermoset systems. Currently, diaphragm formed parts using thermoset composites are in production on Boeing's 777. Thermoset systems possess several advantages over thermoplastics, including lower fabrication temperatures and pressures, and in some cases, lower material costs. Diaphragm materials used with thermoplastics are typically superplastic aluminum alloys or high temperature polymers, whereas high elongation rubbers can be used with thermosets.

The conformance of aligned fiber composites to complex geometries is achieved by various viscous shearing mechanisms. Two important shear modes are longitudinal in-plane shear, where adjacent *fibers* slide past one another, and interply shear where *plies* slide relative to each other. These modes are shown in Figure 2. Some degree of transverse shearing and longitudinal through-the-thickness shearing within a ply is also necessary to form ideal parts.

The major failure modes during forming are; 1) thickness variations, 2) in-plane buckling, where failure occurs on the scale of the fibers or tows, and, the topic of this paper, 3) laminate wrinkling, where compressive forces induced during forming cause a gross buckling deformation through the entire thickness of the laminate (see Figure 3). These compresive forces arise from the significant material compression necessary to form many doubly curved shapes. A simple kinematic argument can be used to illustrate the compressive deformation. For example, Figure 4 shows the preform for a (0/90) laminate used to form a hemisphere. In order to achieve the final part shape, the circumference of the preform must compress to that of the base of the hemisphere. For a circular preform, for example, this requires an ideal circumferential compressive strain of -0.36. This strain must be accommodated by the shearing mechanisms mentioned above, and thus an associated compressive forces would be expected to scale with these shearing stresses. An important simplifying assumption is that in-plane strains lead to in

plane stresses which in turn lead to the in-plane compressive forces. By this reasoning, the through-the-thickness shears, Γ_{13} and Γ_{23}, are of only secondary importance to this failure mode.

2 Scaling Laws for Ideal Composites

In this study, the required ideal shear patterns are determined *a priori* from the part shape by differential geometry theory. With some knowledge of the shear strain mapping and the appropriate constitutive equations for the material deformation behavior, it is then possible to estimate the magnitude of the stresses induced in the composite during forming. This information, in combination with the stiffness properties of the diaphragm and the composite's inherent resistance to buckling, then forms the basis of the wrinkling scaling laws which are presented here.

The critical condition that leads to laminate wrinkling can be developed by using an energy analysis [1]. Figure 5(a) shows a free body diagram for a simplified composite laminate and constraining diaphragm during forming, and Figure 5(b) shows the geometry of a buckled composite. The work of deformation ΔT is given by;

$$\Delta T = P \cdot \Delta \equiv \frac{P\delta^2}{L} \tag{1}$$

The strain energy ΔU of the system is,

$$\Delta U = \Delta U^d + \Delta U^c \tag{2}$$

where the superscripts d & c represent the diaphragm and composite respectively. The strain energy associated with stretching of the diaphragm is given by,

$$\Delta U^d \equiv 2F_D \cdot \Delta \tag{3}$$

and that required for bending of the composite is,

$$\Delta U^c = \int_0^L \frac{M^2}{2EI} dx \cong \frac{P^2 \delta^2 L}{4E(t)I}. \quad (4)$$

The critical load P_{crit} for wrinkling occurs when $\Delta T = \Delta U$, which leads to

$$P_{crit} = 2F_D + \frac{KE(t)I}{L^2} \quad (5)$$

Note that as $t \rightarrow \infty$, $E(t) \rightarrow 0$ and hence $P_{crit} \rightarrow 2F_D$

2.1 Scaling Laws for Compressive Forces

Based upon extensive tests as described in section 4.0, it was found that a general constitutive equation for the composite shearing modes would include a yield stress "τ_o" and a power law shear rate behavior with exponent "n", and coefficient "m". Hence the two principle contributors to the in-plane compressive force can be scaled as,

$$F_{12} \sim N_p hw(\tau_0 + m\dot{\Gamma}_{12}^n) \quad (6)$$

and

$$F_{v3} \sim N_p Lw\left(\tau_0 + m\dot{\Gamma}_{v3}^n\right), \quad (7)$$

and are illustrated in Fig. 6. The labeling system corresponds to the material and part coordinate systems shown in Fig. 7.

3. Ideal Kinematics

The shear strains required in eqs. (6) and (7) can be estimated from ideal kinematics, and the average strain rates can then be estimated by dividing by the forming time. The calculation requires the "ideal" assumption that inter-fiber

spacing and part thickness remains constant [2-4]. Here, we will outline the calculation of Γ_{12} and Γ_{3v}, for two important part shapes; hemispheres and curved C-channels. In general, the required strains for ideal composites can be calculated directly only for relatively simple shapes. More complex shapes would require a properly constructed CAD drawing [2-4]. Briefly, we will calculate Γ_{12} and use the implied displacements to calculate Γ_{3v}. Hence Γ_{12} and Γ_{3v} are closely related.

To determine the in-plane shear Γ_{12}, consider the shear along a fiber element. If a fiber slips a total distance "δ" relative to its neighbor with inter-fiber spacing "h", then the total shear for the fiber can be written as;

$$\Gamma_{12} = \frac{\delta}{h} . \tag{9}$$

This can be related to the geodesic curvature "κ_g" of the fiber by [2, 3],

$$\Gamma_{12} = \int_0^L \kappa_g(s) ds \tag{10}$$

where the fiber is of length L, "s" is measured along the fiber, and we have ignored any "d.c." component of the shear along the entire fiber.

Furthermore, the above integral can be related to the Gaussian (or double) curvature "K" for the part surface over some region "R", enclosed by "M" smooth curves "C_i" with exterior angles "θ_i" (one of them representing the fiber of interest) by the Gauss-Bonnett theorem. See [2,5].

$$\int_C \kappa_g \, ds + \int \int_R K dA = 2\pi - \sum_{i=1}^{M} \theta_i \tag{11}$$

Hence by using this result, the required shear can be determined from the part shape (K) and the fiber orientation (θ_i). This procedure can be used to calculate the required ideal shears for a variety of complex shapes [2].

3.1 Differential Geometry Results for Hemispheres and C-channels

Example 1: Hemisphere

(a) In-plane Shear

We wish to determine the in-plane shear for the fiber identified by the ideal path C_3 in Figure 8. Here the arcs of the closed path C are as follows: C_1 is a semi circle on a great circle; C3 is a semi circle representing the fiber path of interest; and C_2 and C_4 are the connecting arcs that lie on a great circle. The geodesic curvature of arcs C_1, C_2 and C_4 are all zero. The line integral in the Gauss-Bonnet theorem thus reduces to that of the fiber path C_3. The exterior angles sum to 2π, and since the Gaussian or total curvature of the hemisphere is,

$$K = \frac{1}{R^2} \tag{12}$$

the Gauss-Bonnet theorem thus reduces to,

$$-\int_L^0 \kappa_g ds = KA = \frac{1}{R^2}(\pi Rb) = \pi \sin\phi. \tag{13}$$

or

$$\Gamma_{12} = \pi \sin\phi \tag{14}$$

(b) Interply Shear

Knowledge of the in-plane shear pattern for a given part geometry allows the preform shape to be calculated. Figure 9 (a) shows the preform for a hemisphere with an orthogonal grid. Referring to the co-ordinate system with origin at the center of the preform, and considering a 0/90 laminate one can identify a series of points on both the 0° and 90° plies that have the same (X,Y) co-ordinates. These

points will move relative to one another after forming. Figure 9(b) shows the location of the points A and B, after forming. The positions of these points after forming are determined assuming that the individual plies achieve ideal in-plane shear patterns. The relative movement of the points is given by,

$$M = \beta R \tag{15}$$

where R is the radius of the hemisphere, and β is the azimuthal angle between the points (X_1, Y_1, Z_1) and (X_2, Y_2, Z_2). From the dot product of the vectors;

$$\beta = \cos^{-1}\left[\frac{1}{R^2}(x_1x_2 + y_1y_2 + z_1z_2)\right] \tag{16}$$

or

$$\beta = \cos^{-1}\left[\begin{array}{l}\sin\theta_1\cos\theta_2\sin\left(\dfrac{\theta_1}{\cos\theta_2}\right) + \sin\theta_2\cos\theta_1\sin\left(\dfrac{\theta_2}{\cos\theta_1}\right) + \\ \cos\theta_1\cos\theta_2\cos\left(\dfrac{\theta_2}{\cos\theta_1}\right)\cos\left(\dfrac{\theta_1}{\cos\theta_2}\right)\end{array}\right] \tag{17}$$

Fig. 10 shows the relative interply movement for a quadrant of a hemisphere. The maximum occurs when X=Y=0.934R. At this location β = 0.297. Therefore the maximum relative interply movement M_{max} is given by;

$$M_{max} \cong 0.3R \tag{18}$$

This represents a rather large displacement. For example for a 7.5 cm radius hemisphere, the maximum interply movement necessary to form an ideal 0/90 part is on the order of 2.25 cm. This movement is accommodated by the resin rich layer that is found on the surface of most prepreg plies. The shear required is calculated by dividing this relative movement by the thickness of the interply layer, which for most materials is on the order of a few fiber diameters. This calculation yields a value for shear that is on the order of 1,000 or roughly two or three orders of magnitude larger than the in-plane shear.

Example 2: Curved C-Channel

(a) In-plane Shear

Figure 11 shows the kind of c-channel we are concerned with in this work, the two contours are arcs of concentric circles with radii R_1 and R_2. Figure 11 shows the inner flange of radius R_1. Note that the geodesic curvature of the fiber paths is not changed by unrolling the flange onto the flat. We consider the 0^o plies where the fibers run along the length of the c-channel i.e. in the x direction. The appropriate ideal fiber mapping is the one where shear is not required on the top face of the c-channel; all shearing occurs on the flanges. The tangent angle α on the top is duplicated on the flange [3]. Therefore the shear at point P is simply the angle enclosed by the arc, which is α. We can obtain a more general expression for the shear at any point on the flange by considering the geometry shown in Figure 13. The distance between fibers f_o and f_p is,

$$\Delta = R_1(1-\cos\alpha) \tag{19}$$

The distance lateral to the fibers is given by,

$$S_n = \overline{OA_o}$$

Then,

$$\overline{PA} = S_n - \Delta = S_n - R_1(1-\cos\alpha) \tag{20}$$

and the co-ordinates of the point A are given by,

$$x_A = x_p + \overline{PA}\sin\alpha = R_1\alpha + [S_n - R_1(1-\cos\alpha)]\sin\alpha \tag{21}$$

$$y_A = \overline{PA}\cos\alpha = [S_n - R_1(1-\cos\alpha)]\cos\alpha \tag{22}$$

The length of the fiber segment A_o-A is given by,

$$l_f = \int_o^{\alpha} \sqrt{\left(\frac{dx_A}{d\alpha}\right)^2 + \left(\frac{dy_A}{d\alpha}\right)^2}\, d\alpha. \tag{23}$$

Therefore the shear at any location along the fiber on the inner flange can be related to the fiber length by the expression,

$$l_f = 2R_1 \sin\Gamma_{12} + (S_n - R_1)\Gamma_{12}. \tag{24}$$

A similar analysis yields the following expression for the outer flange;

$$l_f = 2R_1 \sin\Gamma_{12} + (S_n - R_1)\Gamma_{12} \tag{25}$$

When R_1 (or R_2) and s_n are known, for any given fiber length we can calculate the shear using Newton's iterative method. A useful result however, is that the maximum shear required to form a c-channel is simply the angle of the enclosing arc α.

Figure 14 shows an ideal fiber mapping for a 90° ply where in-plane shear is allowed on the top face. This is consistent with some experimental observations for large parts. From kinematics again the maximum in-plane shear required is simply α. To determine the interply shear, however we need to know the positions of all fibers after forming. Referring to the co-ordinate system given, the parametric equations describing the curve P-B are,

$$x = R_1 \cos\theta_1 - R_1(\alpha_1 - \theta_1)\sin\theta_1$$

$$y = R_1 \sin\theta_1 + R_1(\alpha_1 - \theta_1)\cos\theta_1 \tag{26}$$

For the outer flange the equations for C-D are (see Figure 15),

$$u = R_2\theta_2 + R_2(\sin\alpha_2 - \sin\theta_2)\cos\theta_2$$

$$v = R_2(\sin\alpha_2 - \sin\theta_2)\sin\theta_2 \tag{27}$$

(b) Interply Shear

The fiber mapping for a 0/90 layup on the inner flange of a curved c-channel is shown in Figure 16. The relative interply movements between the plies at point A in the 0° and 90° fiber directions are denoted δ_0 & δ_{90}. It can be shown that [6].

$$\begin{aligned}\delta_0 &= l_f - (R_1\alpha + \overline{PA}\sin\alpha) \\ &\approx \frac{1}{6}(R_1 + s_n)\alpha^3 \\ &\approx \frac{1}{6}R_1\alpha^3,\end{aligned} \tag{28}$$

and

$$\begin{aligned}\delta_{90} &= \frac{R_1}{2}\left(\alpha + \frac{\overline{PA}\sin\alpha}{R_1}\right)^2 + \overline{PA}\cos\alpha - s_n \\ &\approx \frac{1}{2}s_n\frac{R_1 + s_n}{R_1}\alpha^2 \\ &\approx \frac{1}{2}s_n\alpha^2.\end{aligned} \tag{29}$$

Hence the relative displacement between 0° and 90° plies at point A is:

$$\begin{aligned}(\delta_{int})_A &\approx \sqrt{\delta_0^2 + \delta_{90}^2} \\ &\approx \sqrt{(\frac{1}{6}R_1\alpha^3)^2 + (\frac{1}{2}s_n\alpha^2)^2} \\ &= \frac{1}{6}\alpha^2\sqrt{R_1^2\alpha^2 + 9s_n^2}.\end{aligned}$$

For the outer flange, for a point where in-plane shear of a 0 degree fiber is α, a similar analysis leads to the following result:

$$\delta_{int} \approx \frac{1}{6}\alpha^2\sqrt{R_2^2\alpha^2 + 9s_n^2}.$$

For the example of a curved c-channel that is 61 cm long and has an 244 cm inner radius, the in-plane shear is approximately 0.125, while the maximum relative

movement between the plies is on the order of 0.11 cm. Dividing the latter by a typical interply spacing yields an interply shear value on the order of 50.

4.0 Material Rheology

The shearing behavior of the aligned graphite fiber/epoxy prepregs was characterized by a three point bending test which produced a through-the-thickness shear. By assuming the material is transversely isotropic, and by adding multiple plies to add interply effects, one can measure the Γ_{13} and Γ_{12} material response directly, and infer the $\Gamma_{\nu 3}$ response [7,8]. The test configuration and typical results for AS4/3501-6 prepreg tested at different rates of deformation are shown in Figure 17. The tests were carried out in an Instron 1125 mechanical test machine. All results show a transient rise in stress followed by a steady state. The rise time was on the order of 1 sec. for the slower cross-head speeds with a sample length of 5 cm. (Note that in general the rise time depends upon the square of the sample length, see [9]). The average strain rate dependence can be observed, for example, by plotting the maximum force at steady state vs the maximum shear rate, as shown in Fig. 18. These results show a power law rate dependence at low temperatures and high shear rates, and a significant reduction in rate and temperature effects at high-temperatures and/or low shear rates. Apparently, the material behavior is dominated by the polymer in the former regime, and the fiber network in the later. For example, time shifting the data shown in Fig. 18 shows a distinct deviation from the WLF equation at high temperatures and low shear rates. From these results an effective power law viscosity can be estimated for high rate and low temperature regime, and an effective yield stress can be estimated in the high temperature and/or low rate regime. The addition of multiple plies showed that the effective in-plane viscosity and the inter-ply viscosity are comparable at low shear rates (within 10%). The apparent shear viscosity for the Hercules AS4/3501-6 for various temperatures and cross-head speeds is shown in Figure 19. More details concerning the rheology of these systems will be available in a forthcoming paper [8].

5.0 Laminate Buckling Resistance

The forces that oppose wrinkling deformations originate from the inherent resistance of the material itself and from the restraining force supplied by diaphragm as it is stretched. The trends in the wrinkling data consistently suggest that even without the support of a diaphragm, the composite material can resist wrinkling to some extent. In an effort to evaluate this inherent wrinkling resistance, a number of buckling tests on cross-plied samples were carried out. The test geometry was based on an Euler buckling test column with fixed ends. Samples were either 8 or 16 plies thick and the test direction was chosen to be that which was weakest i.e. in the 45° direction on a [0/90] laminate and at 22.5° on a [0/90/±45] layup. Samples were loaded instantaneously and were deemed to be wrinkled when a lateral deflection of 6 mm was reached. Results of room temperature (22°C) buckling tests are shown in Figure 20. The critical Euler buckling load for this test geometry is given by;

$$P_{crit} = \frac{4\pi^2 E(t) I}{L^2} \qquad (30)$$

where,

I = moment of inertia
L = Length of column
E(t) = time dependent stiffness of the composite material

The results show the clear time dependence to the buckling resistance of the material. The effective stiffness of the laminates in the flat region of the curve is on the order of ~7 MPa (10^3 psi).

To estimate the buckling resistance supplied by the diaphragm requires estimation of the diaphragm tension transverse to the potential buckle as given in eq. (5). This in turn can be estimated from a knowledge of the diaphragm strain during forming, and its constitutive behavior. To determine the critical diaphragm strains a grid pattern was printed on the diaphragm and the deformations measured

after forming. For hemispheres the critical diaphragm strain is in the circumferential direction, while for curved C-Channels, it is along the length of the flange.

For the purposes of calculating diaphragm tension forces we designate the critical stress direction (transverse to the potential wrinkle) as σ_{11}. The generalized expression for the stress in the 1 direction for biaxial tension of a rubber membrane is given by [10];

$$\sigma_{11} = 2\left(\lambda^2{}_1 - \frac{1}{\lambda_1^2\lambda_2^2}\right)\left(\frac{\partial U}{\partial I_1} + \lambda_2^2\frac{\partial U}{\partial I_2}\right), \tag{31}$$

where U is the strain energy function for an elastic solid. The invariant terms I_1 & I_2 are given by;

$$I_1 = \lambda_1^2 + \lambda_1^2 + \lambda_1^2$$

$$I_2 = \frac{1}{\lambda_1^2} + \frac{1}{\lambda_2^2} + \frac{1}{\lambda_3^2}$$

From conservation of volume,

$$\lambda_1\lambda_2\lambda_3 = 1,$$

Hence,

$$\lambda_1 = \frac{1}{\lambda_2\lambda_3} = \frac{A_o}{A}, \tag{32}$$

where A_O and A correspond to the original and current cross sectional area of the diaphragm. We can therefore write an expression for the nominal stress in the 1 direction as;

$$\sigma_{11}^{*} = 2\left(\lambda_1 - \frac{1}{\lambda_1^3\lambda_2^2}\right)\left(\frac{\partial U}{\partial I_1} + \lambda_2^2\frac{\partial U}{\partial I_2}\right) \tag{33}$$

A similar expression can be derived for the nominal stress in the 2 direction;

$$\sigma_{22}^{*} = 2\left(\lambda_2 - \frac{1}{\lambda_1^2\lambda_2^3}\right)\left(\frac{\partial U}{\partial I_1} + \lambda_1^2\frac{\partial U}{\partial I_2}\right) \tag{34}$$

In biaxial testing λ_1 & λ_2 can be varied appropriately to fix the invariant terms and the relevant partial derivatives of the strain energy function, U, can be evaluated. For convenience we can rewrite Equation 33 as;

$$\sigma_{11}^{*} = \left(\lambda_1 - \frac{1}{\lambda_1^3\lambda_2^2}\right)\left(1 + \frac{\lambda_2^2}{k}\right)\sigma_0 \tag{35}$$

Where;

$$\sigma_0 = 2\frac{\partial U}{\partial I_1}$$

$$\frac{1}{k} = \frac{\partial U / \partial I_2}{\partial U / \partial I_1}$$

Rivlin and Saunders [11] determined the appropriate quantities for vulcanized rubber They found that $\partial U / \partial I_1$ is approximately constant and independent of I_1 & I_2. $\partial U / \partial I_2$ is independent of I_1 but is a linear function of I_2. 1/k is thus a weak linear function of I_2 only. Thus from Rivlin and Saunders data;

$$\frac{1}{k} = 0.152 - 0.00368 \times I_2 \tag{36}$$

For uniaxial tension,

$$\lambda_2 = \lambda_3 = \frac{1}{\sqrt{\lambda_1}} \tag{37}$$

and Equation 35 can be rewritten,

$$\sigma_{11}^{*} = \left(\lambda_1 - \frac{1}{\lambda_1^2}\right)\left(1 + \frac{1}{k\lambda_1}\right)\sigma_0 \tag{38}$$

Diaphragm Thickness (mm)	0.397	0.794	1.588	3.175
σ_0 (kN/m^2)	574	745	896	952

Table 1. σ_0 for different thickness diaphragms, from uniaxial test data.

We can now fit Equation 38 to uniaxial test data for the different thicknesses of silicone rubber diaphragms to determine the values of the the constant σ_0. These values are shown in Table 1. Agreement between the tests and the model is shown in Figure 21.

Table 2 shows measured values for the extension ratios for formed hemispheres of different sizes. It also shows the constants and invariants needed to calculate σ_{11}* from Equation 38. Note that λ_1 is circumferential extension close to the edge of the part and λ_2 is measureed in the orthogonal direction at the same location.

	λ_1	λ_2	λ_3	I_2	1/k
Hemisphere R=5.1 cm	1.03	2.25	0.43	6.48	0.13
6.4 cm	1.04	2.50	0.38	7.87	0.12
8.9 cm	1.17	2.85	0.31	11.54	0.11
11.4 cm	1.29	3.10	0.25	16.60	0.09
C-Channel L=30.5 cm	1.22	2.25	0.36	8.40	0.12
61.0 cm	1.02	1.42	0.69	3.55	0.14
121.9 cm	1.09	1.68	0.55	4.55	0.14

Table 2. Extension ratios and material constants for the deformation of silicone rubber diaphragm material over hemispheres of different sizes.

The diaphragm tension force is then simply;

$$F_D = Dw\sigma_{11}^* \tag{39}$$

where D is the undeformed thickness of the diaphragm, and w is the width.

6 Order of Magnitude Analysis

In this section, we will employ an order-of-magnitude analysis to estimate the relative importance of F_{12} vs F_{3v}, and $2F_D$ vs. the buckling resistance of the composite.

Consider an element of the buckled laminate, as shown in Figure 22. L is the specific length of a wrinkled region (in the critical direction which is perpendicular to the wrinkle); w is the width of the region (parallel to the wrinkle). Both of these dimensions scale with the size of the part. The number of plies is N_p, and the thickness of each ply is H.

Then, the ratio of inter-ply and in-plane viscous shear forces can be estimated by:

$$\frac{F_{v3}}{F_{12}} \sim \frac{N_p L w m \dot{\Gamma}_{v3}^n}{N_p H w m \dot{\Gamma}_{12}^n} \sim \frac{L \dot{\Gamma}_{v3}^n}{H \dot{\Gamma}_{12}^n} \sim \frac{L}{H}\left(\frac{\Gamma_{v3}}{\Gamma_{12}}\right)^n. \tag{40}$$

We know that:

$$H \sim 10^{-3} \text{ cm},$$
$$\frac{\Gamma_{v3}}{\Gamma_{12}} \sim 10^{2 \text{ to } 3},$$
$$n \sim 0 \text{ to } 0.45$$

For a part of dimension $L \sim 10^0$ cm., this leads to

$$\frac{F_{v3}}{F_{12}} \sim \frac{L}{H}\left(\frac{\Gamma_{v3}}{\Gamma_{12}}\right)^n \sim \frac{10^0}{10^{-3}} \cdot \left(10^{2 \text{ to } 3}\right)^{0 \text{ to } 0.45} \sim 10^3 \text{ to } 10^4. \tag{41}$$

Hence, according to this analysis, the interply viscous shear stress is the main source of compressive force within a laminate.

The relative magnitude of the two resistance forces is approximated by:

$$\frac{F_D}{F_{elastic}} \approx \frac{12Dw\sigma_{11}^* L^2}{4\pi^2 E(t) w N_p^a H^3} = \frac{3D\sigma_{11}^* L^2}{\pi^2 E(t) N_p^a H^3}. \tag{42}$$

Since

$$D \sim 10^{-2} \text{ cm},$$
$$\sigma_{11}^* \sim 10^5 \text{ Pa},$$
$$L^2 \sim 10^1 \text{ cm}^2,$$
$$E(t) \sim 10^6 \text{ Pa, (room temperature)}$$
$$N_p \sim 10^0 \text{ to } 10^3,$$
$$H^3 \sim 10^{-6} \text{ cm}^3,$$

we get

$$\frac{F_D}{F_{elastic}} \sim 10^1 \text{ to } 10^4. \tag{43}$$

Hence, diaphragm tension provides the main support against laminate wrinkling.

7. Forming Experiments

To demonstrate the general validity of these scaling laws a series of experiments were conducted, and then each point was plotted in terms of the diaphragm tension F_D and the relative compressive force F_{v3}. This is shown in Figure 23 for a series of [0/90] hemispheres. The range of forming and part parameters is given in Table 3 [6]. As can be seen, a relatively clear demarcation between "good" and "wrinkled" parts exists. Detailed observations on these parts

Variable	Lower Limit	Upper Limit
Temperature	20°C	95°C
Forming Time	1.5 min.	4 hrs
Diaphragm Thickness	0.04 cm	0.159 cm
Diaphragm Strain	1.03	1.3
Number of Plies	2	32
Radius	0.97 cm	11.5cm

Table 3 Parameter ranges for experiments on hemispheres.

revealed, however, that the shear patterns deviated from ideal. For example, the total fiber shears for a series of hemispheres of different sizes is shown in Figure 24. The basic trend is that the fibers follow the ideal shear up to about half way down the side of the part. Toward the edge, the fibers deviate substantially from the ideal. Furthermore, there is a clear size effect; larger parts obtain larger shears. Since, the fibers for $S_n > S_{n,max} > 0.5$ are all shorter than the central fibers the two effects are related.

In a separate set of experiments, a series of curved C-channels with the range of parameters listed in Table 4 were formed [6]. In this case, the preform was constructed with [0/90/±45] ply orientations. This arrangement is substantially more difficult to form than the [0/90] or [±45] arrangements with the same number of plies. The reason for this is related to the additional constraints imposed by the [0/90/±45]. That is, the [0/90] and [±45] arrangements can deform by a trellising type of deformation which substantially reduces the required interply shear.* However, for the [0/90/±45] lay-up this ability to avoid large interply displacements is severely restricted. As a consequence the in-plane compressive force appears to increase by about an order of magnitude. Evidence of interply shear for a [0/90/±45] C-channel and the lack of it for a [0/90] is shown in Figure 25.

* In fact, the fiber path deviations from ideality which we noted in an earlier paper [3] for [0/90] hemispheres, turn out to almost exactly equal to the required interply displacement given by eq. (18).

Variable	Lower Limit	Upper Limit
Temperature	20°C	95°C
Forming Time	1.5 min.	1 hr
Diaphragm Thickness	0.04 cm	0.159 cm
Diaphragm Strain	1.05	1.8
Number of Plies	2	32
Length	30.5 cm	121.9 cm
Web Width	5.1 cm	20.3 cm
Flange Length	5.1 cm	20.3 cm

Table 4 Parameter ranges for experiments on c-channels.

This data is shown in Figure 26. Again a clear organization between good and wrinkled parts is apparent. In this case, however, all of the parts are of the same size. When larger C-channels (scaled up by a factor of 2 in every dimension, but with the same enclosed angle 2α) where formed they did not superimpose on Figure 26. In short, the larger C-channels were harder to make than the small ones by a factor larger than that suggested by our previous scaling laws. This difference appears to be due to a shift in the shear patterns for the small and large parts as shown in Figure 27. For small parts significant shear in the web is allowed, whereas for the large parts all of the shear occurs in the flanges. The pattern for the large C-channel is similar to the ideal shear shown in the figure, but at a reduced level. The large part data can be superimposed if Equation 18 is multiplied by an additional empirical length scale as given in Equation 44. A new plot using the empirical length scale for both large and small C-channels is shown in Figure 28.

$$F_{v3} = LN_{pLW}(\tau_0 + m\dot{\Gamma}^n_{v3})\left(\frac{L}{L_{char}}\right)^2 \qquad (44)$$

8 Thermoplastic Versus Thermoset Diaphragm Forming

Although similar in their basic deformation mechanics, differences in rheology, diaphragm tension, and forming cycle create different failure trends for thermoplastic vs thermoset diaphragm formed composites. For example, while it has been observed that diaphragm formed thermoplastic composites can suffer thickness changes on the order of 17 to 200% [12], generally the variation in thermoset parts is less. For example, some thickness data for thermoset hemispheres and curved C-channels is given in Figs. 29 and 30. These show a variation on the order of ±5-7% before and after autoclave cure. Such variation is typical of parts produced on one sided tooling. The large thickness changes for thermoplastic parts are due primarily to higher diaphragm stiffnesses, which require significantly higher forming pressures to make complex parts. This is shown in Figure 31, where, using the results of Mallon [12,13], the stress/extension ratio behavior of two diaphragms used in thermoplastic forming are compared with a diaphragm used in thermoset forming. As a consequence, to form thermoplastic parts, pressures on the order of 0.1 to 1.7 MPa are used versus vacuum only (0.1 MPa) for thermosets. These differeences in pressures also lead to substancially simpler equipment for thermoset forming. It should be noted, however, that the stiffer diaphragms used with thermoplastics can aid significantly in reducing wrinkling of the part. This can lead to an advantage when forming parts of significant double curvature. Nevertheless, the diaphragm process used with thermosets can produce a wide range of complex shaped parts. Some of these are shown in Figure 32. Furthermore, by selectively adding stiffening reinforcements to the diaphragm, the range of part size and shape can be significantly extended without inducing excessive thickness changes [14].

9 Summary and Conclusions

This paper outlines the basic issues which control laminate wrinkling during the diaphragm forming process. Scaling laws based on the assumption of ideal kinematics show good general agreement with the experiments under limited part size variation. Furthermore deviation from the scaling laws can be traced to trends observed in deformation kinematics. In particular, a significant part size effect on the resulting kinematics is observed, and an empirical scaling law for this effect is proposed.

10. References

1. S.P. Timoshenko and J.M. Gere, Theory of Elastic Stability, 1961, Mc-Graw-Hill, 2nd edition.

2. A.S. Tam and T.G. Gutowski, "The Kinematics for Forming Ideal Aligned Fibre Composites into Complex Shapes", *Composites Manufacturing*, Vol. 1, No. 4, Dec., 1990, pp. 219-228.

3. T. Gutowski, et al, "Differential Geometry and the Forming of Aligned Fibre Composites", *Composites Manufacturing*, Vol. 2, No. 3/4, 1991, pp. 147-152.

4. K. Golden, T.G. Rogers and A.J.M. Spencer, "Forming Kinematics of Continuous Fibre Reinforced Laminates", *Composites Manufacturing*, Vol. 2, No. 3/4, 1991, pp. 267-277.

5. D.J. Struik, Lectures on Classical Differential Geometry, 1961, Dover, 2nd edition.

6. H. Li, "Preliminary Forming Limit Analysis for Advanced Composites", M.S. Thesis, Department of Mechanical Engineering, 1994.

7. E.T. Neoh, "Drape Properties of Thermosetting Prepregs", M.S. Thesis, Department of Mechanical Engineering, M.I.T. 1992.

8. T. Gutowski, G. Dillon, E.T. Neoh, S. Chey, and H. Li, "The Bending Behavior of Thermoset Prepregs", in preparation.

9. A.S. Tam and T.G. Gutowski, "Ply-Slip During the Forming of Thermoplastic Composite Parts", *Journal of Composite Materials*, Vol. 23, June 1989.

10. I.M. Ward, Mechanical Properties of Solid Polymers, 1971, Wiley and Sons, 2nd edition.

11. R.S. Rivlin and D.W. Saunders, Phil. Trans. of the Royal Society A, Vol. 243, p 251, 1951.

12 M.R. Monaghan, P.J. Mallon, C.M. O'Bradaigh and R.B. Pipes, "The Effect of Diaphragm Stiffness on the Quality of Diaphragm Formed Thermoplastic Composite Components" *Journal of Thermoplastic Composites*, Vol. 3, 1990, pp202-215.

13 M.R. Monaghan and P.J. Mallon, "Study of the Mechanical Behaviour of Diaphragm Films", *Composites Manufacturing*, Vol. 2, No. 3/4 1991, pp197-202

14 T.G. Gutowski, G. Dillon, H. Li and S. Chey "Method and System for Forming a Composite Product from a Thermoformable Sheet", United States Patent Application Serial Number 08/203/797.

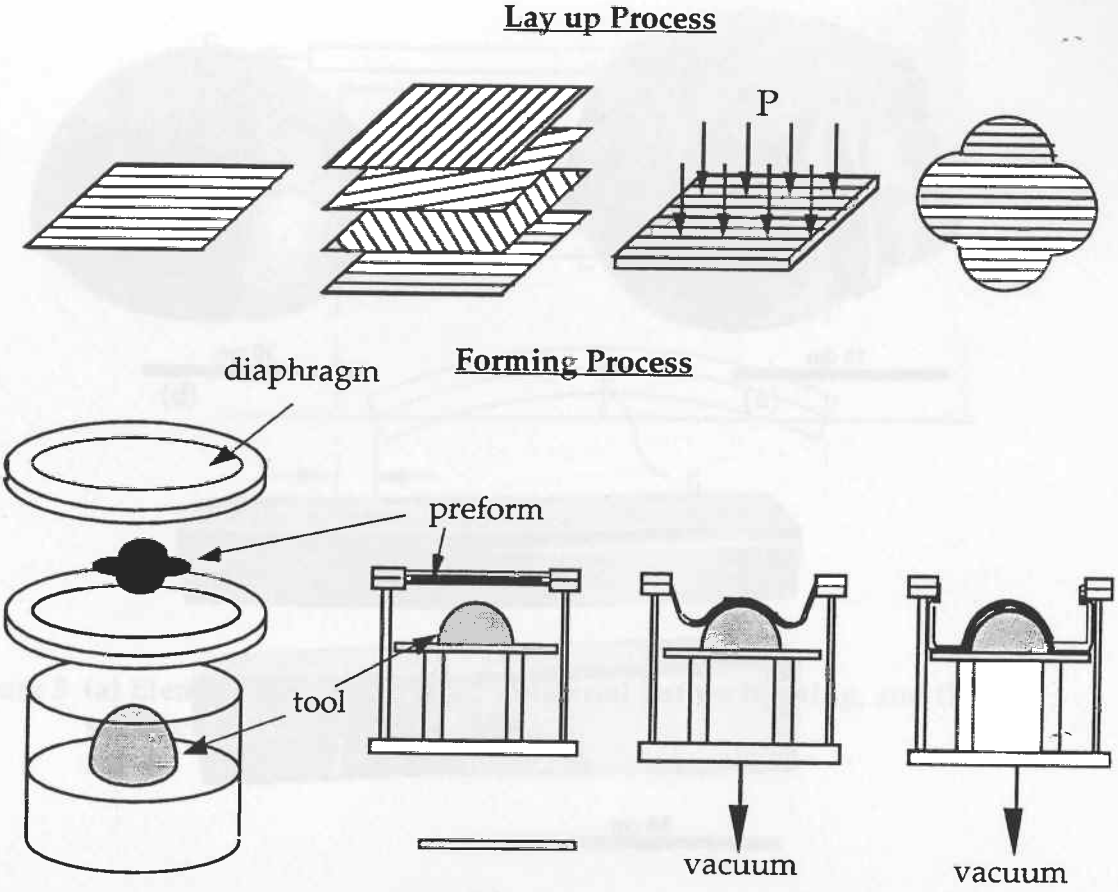

Figure 1 Schematic representation of the diaphragm forming process.

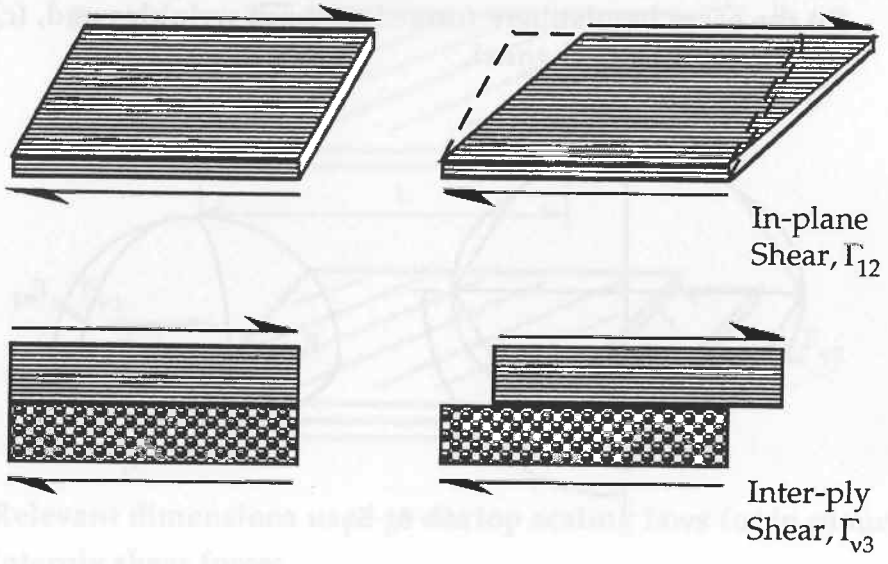

Figure 2 Schematic illustrations of the in-plane and inter-ply shear modes for aligned fiber, cross-plied composites.

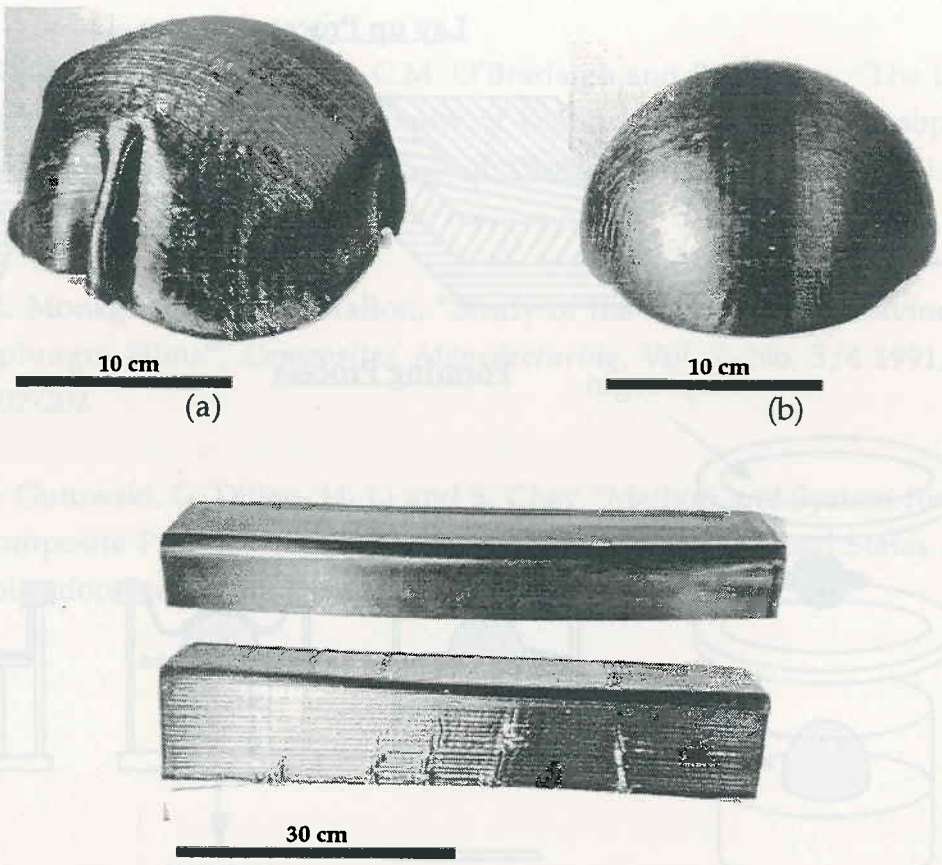

Figure 3 (a) Illustration of laminate wrinkling on a 16 ply 0/90 hemisphere, (b) the same hemisphere formed without wrinkles and, (c) laminate wrinkling on a C-channel.

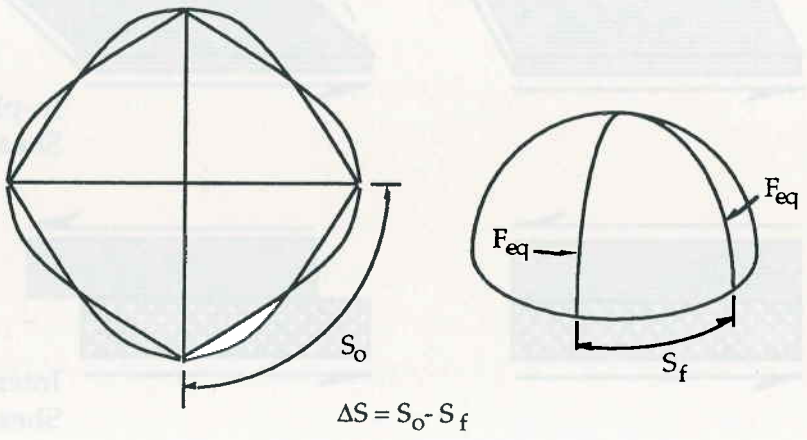

Figure 4 Illustration of the compressive deformation ΔS required to form a hemisphere.

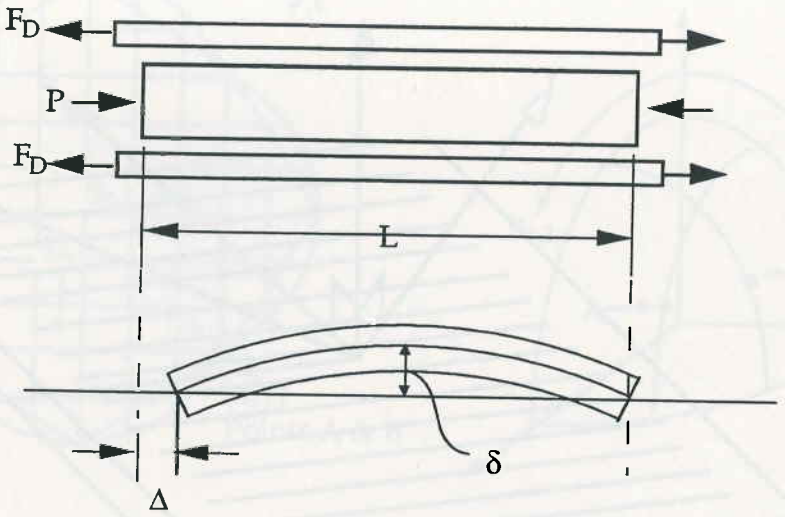

Figure 5 (a) Element of composite and material before forming, and (b) the same element after deformation.

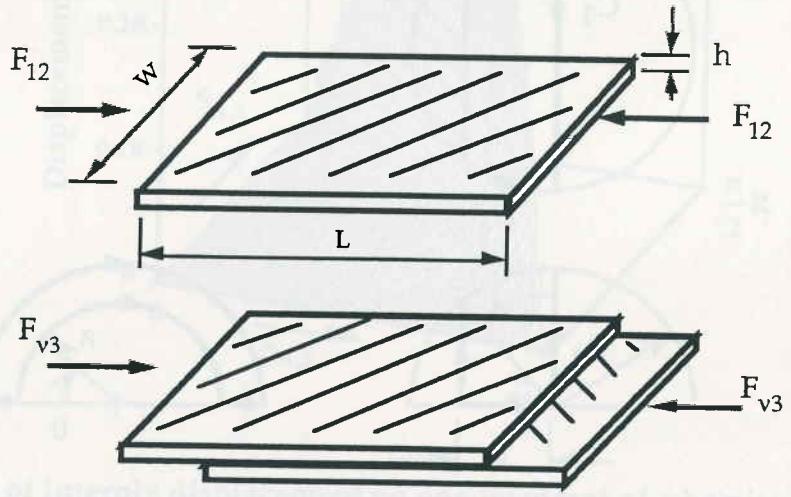

Figure 6 Relevant dimensions used to devlop scaling laws for in plane and interply shear forces.

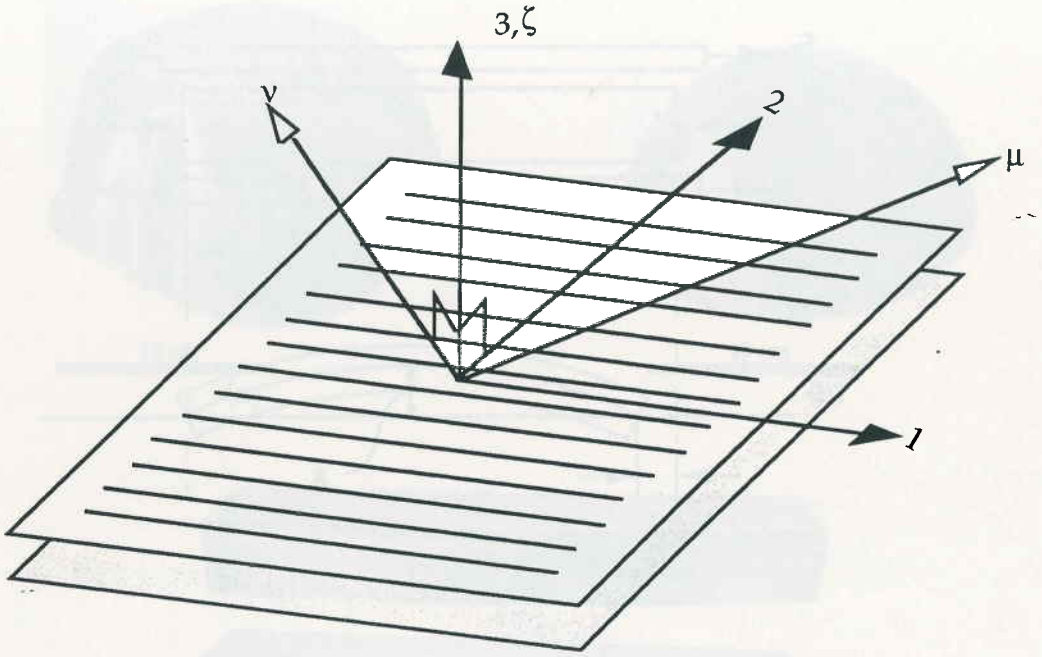

Figure 7 **Illustration of the material co-ordinate system, 1, 2,3 , and part co-ordinate system, μ, ν, ζ.**

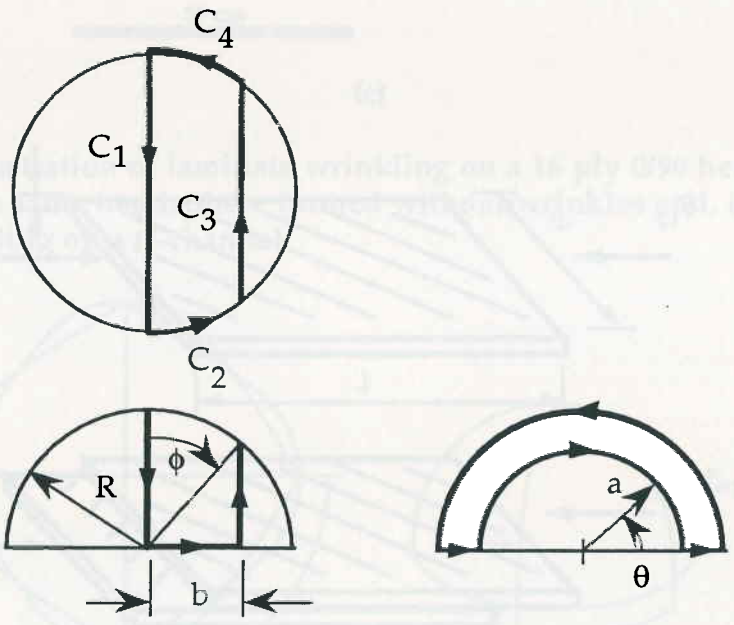

Figure 8 **Illustration of fiber paths on a hemisphere.**

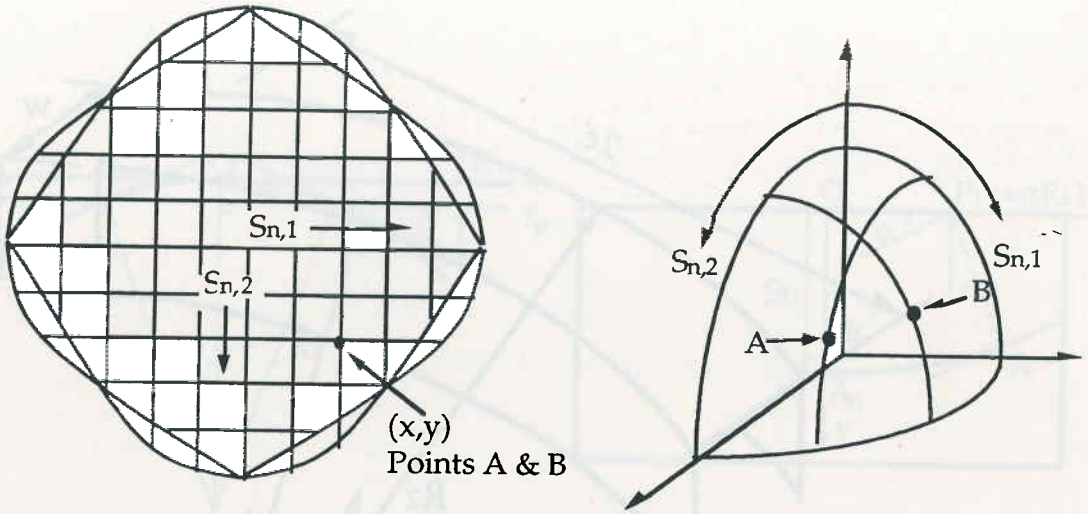

Figure 9 (a) Preform shape for a 0/90 hemisphere, and (b) quadrant of formed part showing the relative motion of points A & B.

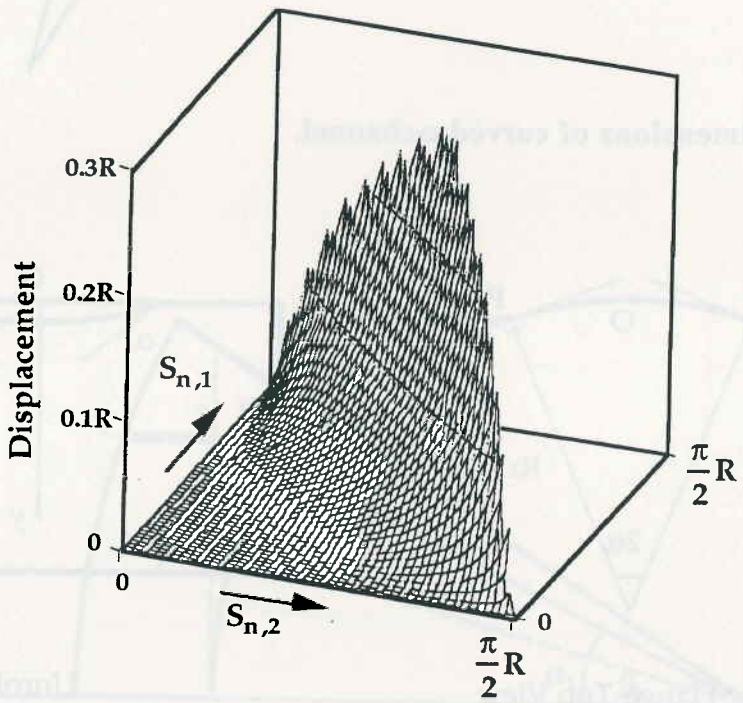

Figure 10 Plot of interply displacement on one quadrant of a hemisphere.

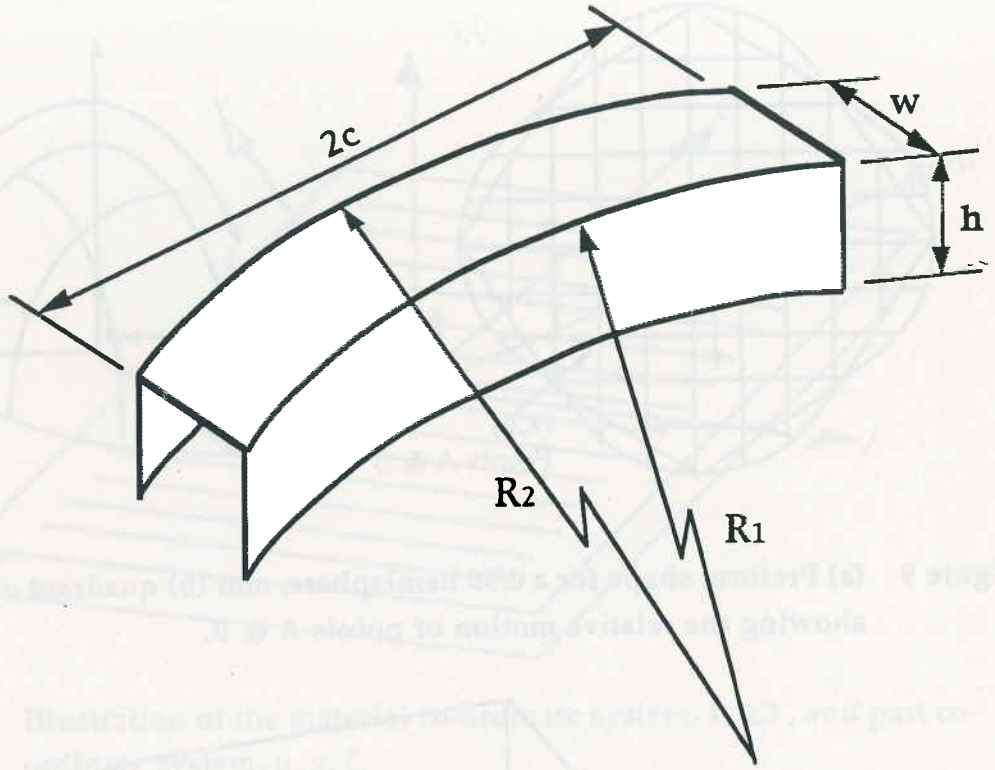

Figure 11 Dimensions of curved c-channel.

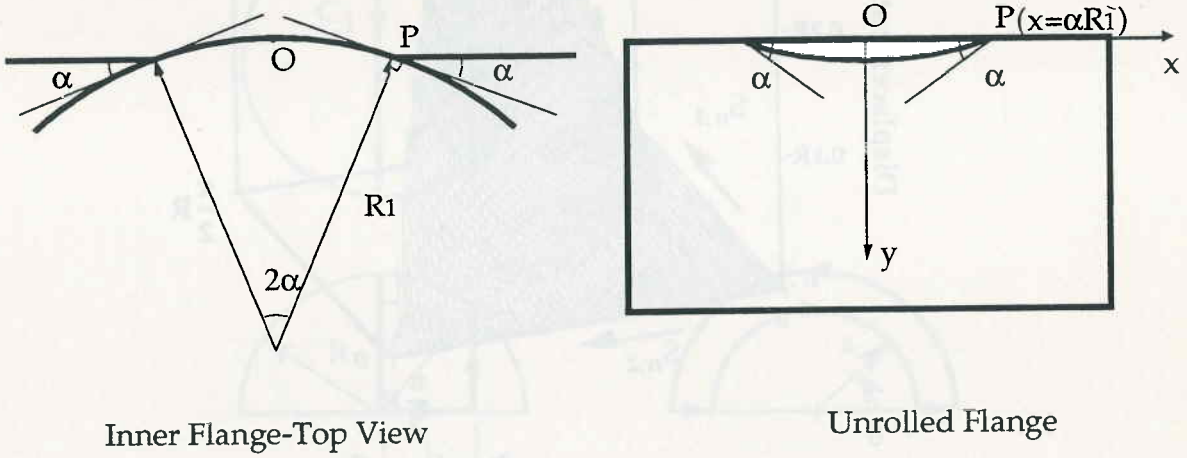

Inner Flange-Top View

Unrolled Flange

Figure 12 Illustration of a fiber path that passes along both the top and the inner flange of a curved c-channel.

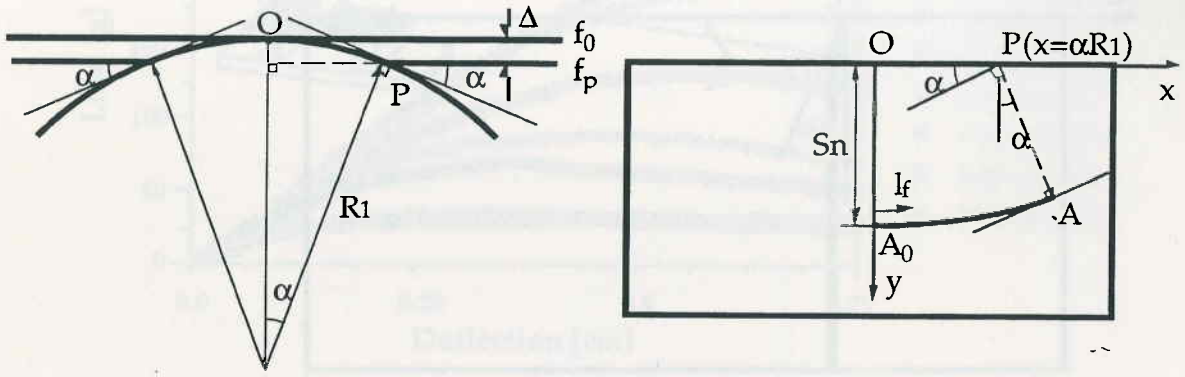

Figure 13 Parameters used to determine the shear along a fiber segment, A-A_o, on the inner flange of a curved c-channel.

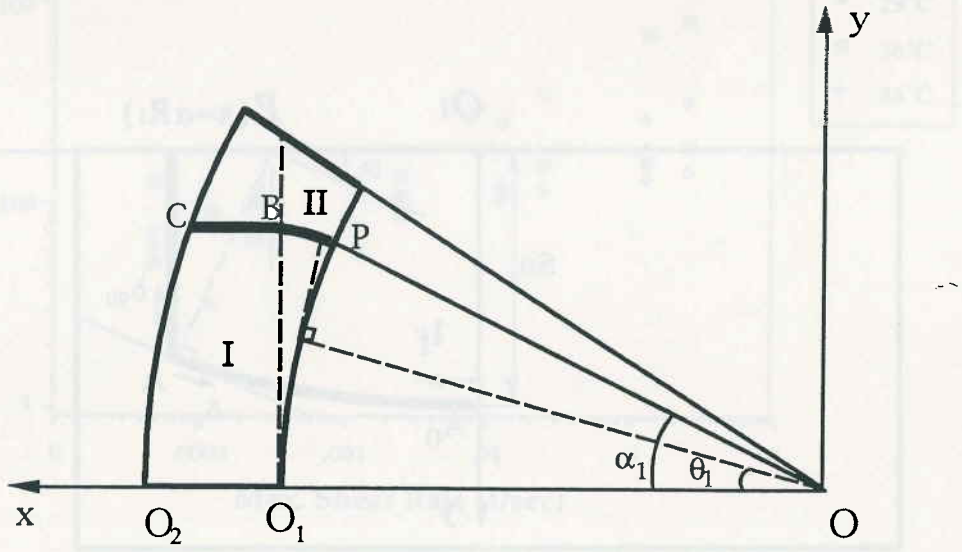

Figure 14 Top view of a c-channel 90° mapping.

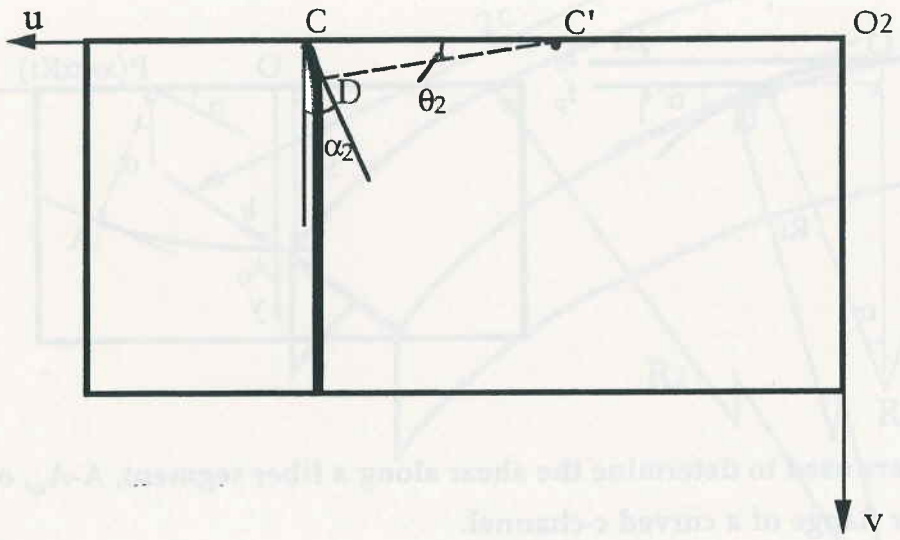

Figure 15 C-channel 90° mapping: outer flange .

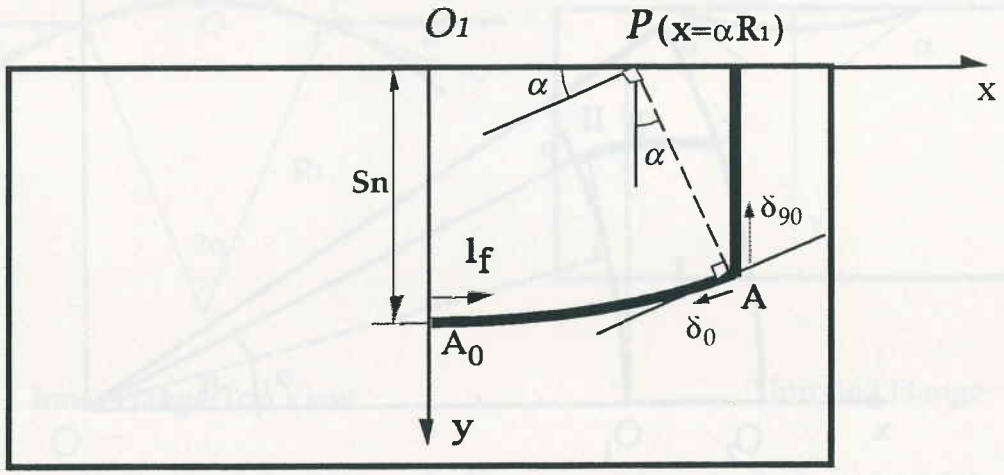

Figure 16 Illustration of inter-ply displacement at point A on the inner flange of c-channel.

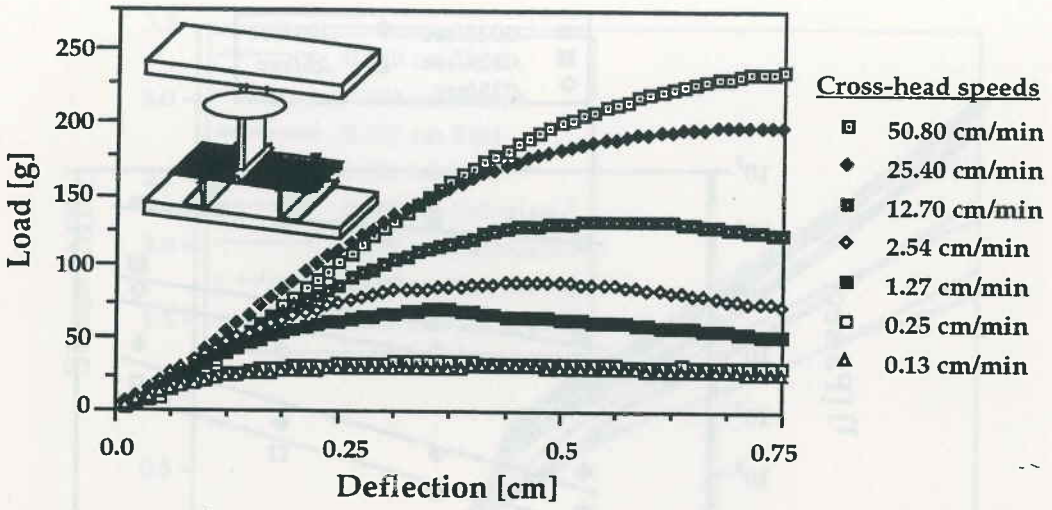

Figure 17 Drape test data for AS/3501-6 graphite/epoxy material tested at different deflection rates.

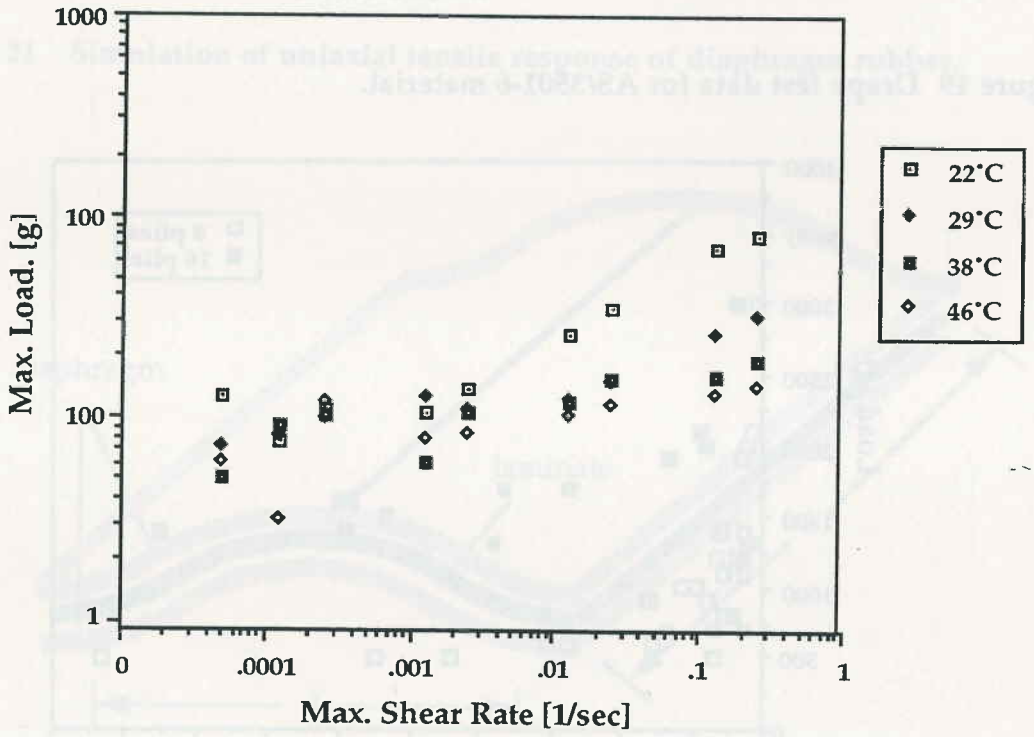

Figure 18 Strain rate dependance of maximum load for drape testing of AS/3501-6 graphite/epoxy material tested at different temperatures.

Y-Scale shifted by 10^3
(was it Fig 18 or Fig 19?)

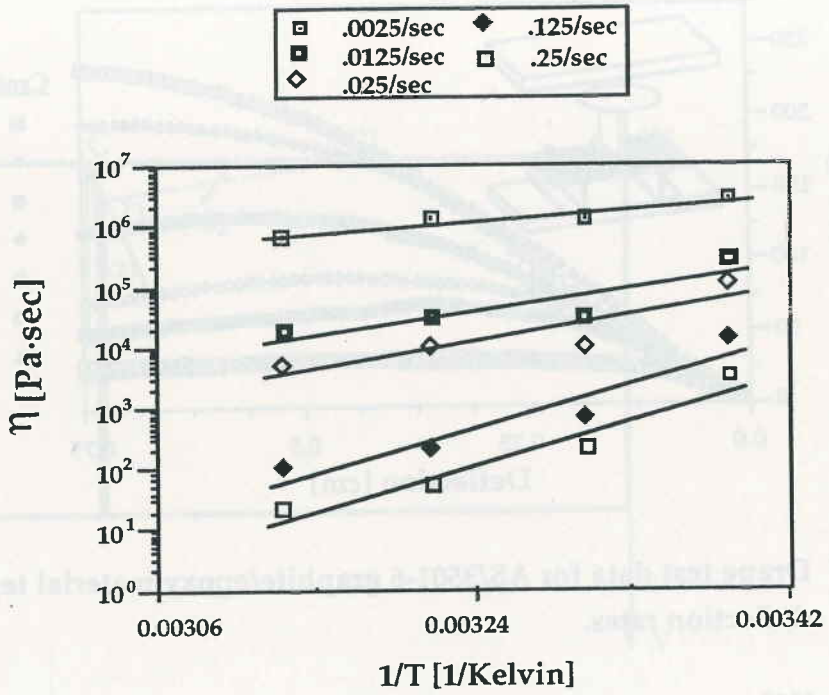

Figure 19 Drape test data for AS/3501-6 material.

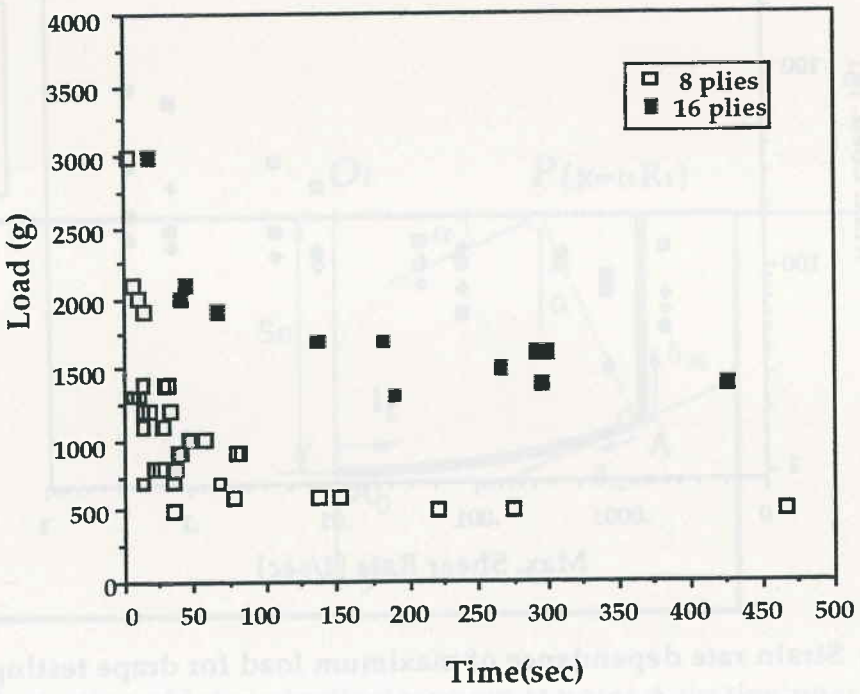

Figure 20 Buckling data for AS4/3501-6 prepreg material.

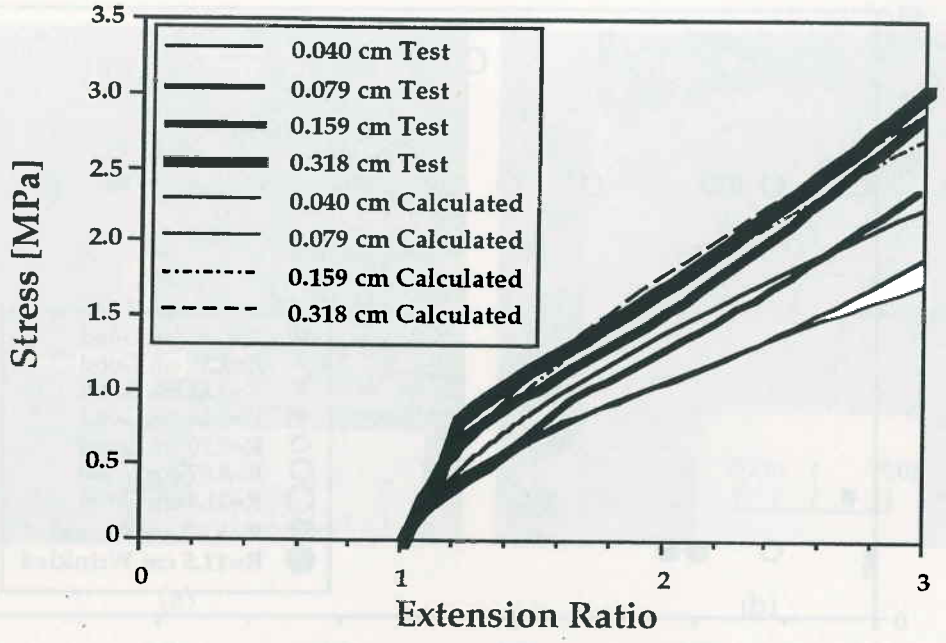

Figure 21 **Simulation of uniaxial tensile response of diaphragm rubber.**

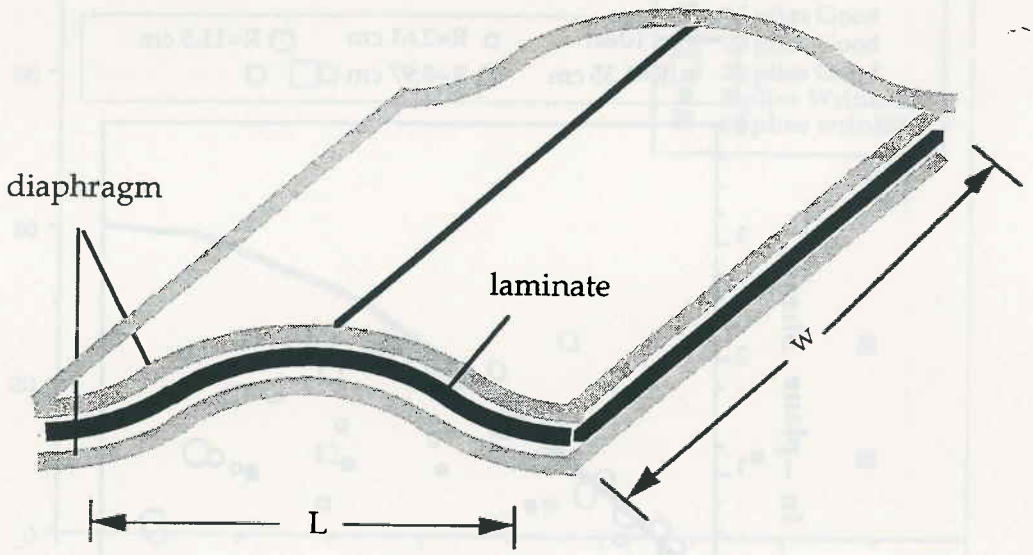

Figure 22 **Illustration of an element in wrinkled region.**

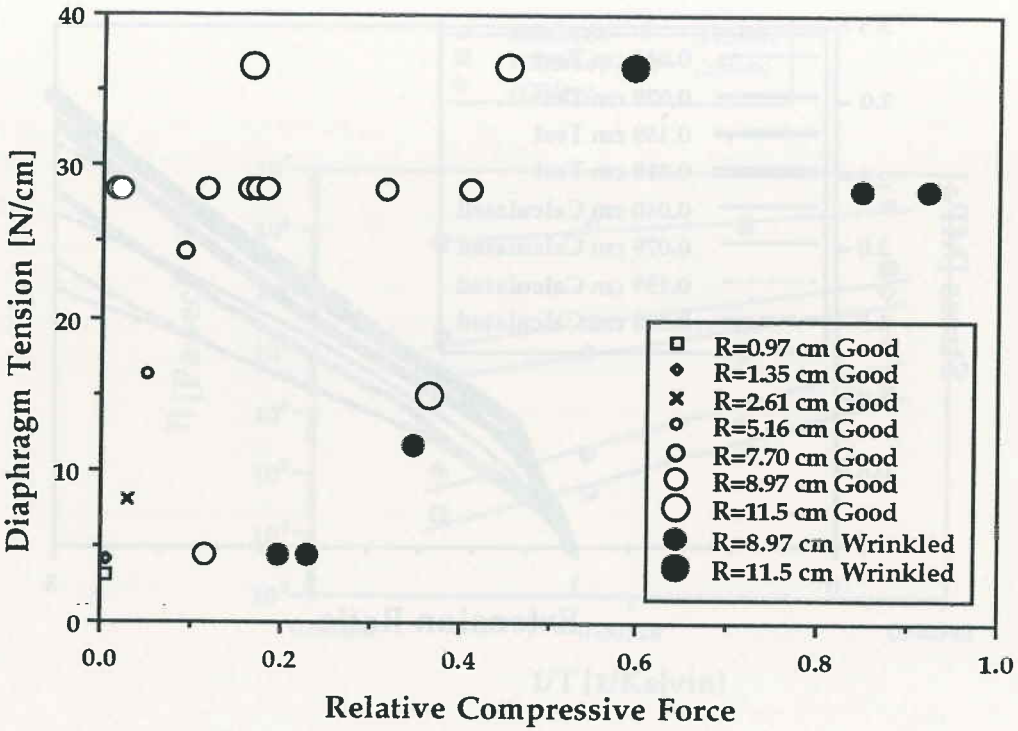

Figure 23 Forming limit diagram based on a simple viscous model for (0°/90°) hemispheres.

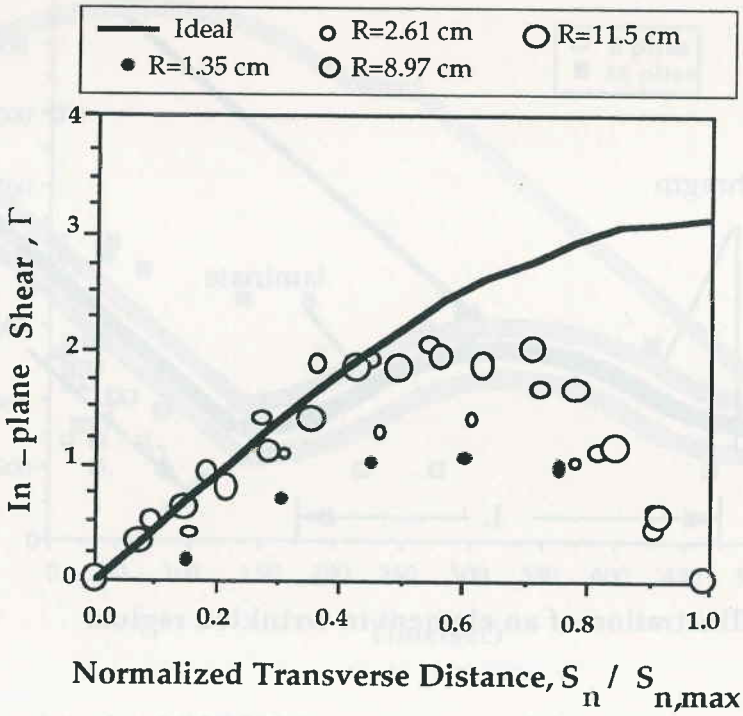

Figure 24 Comparison of ideal fiber and actual fiber shears for (0/90) hemispheres.

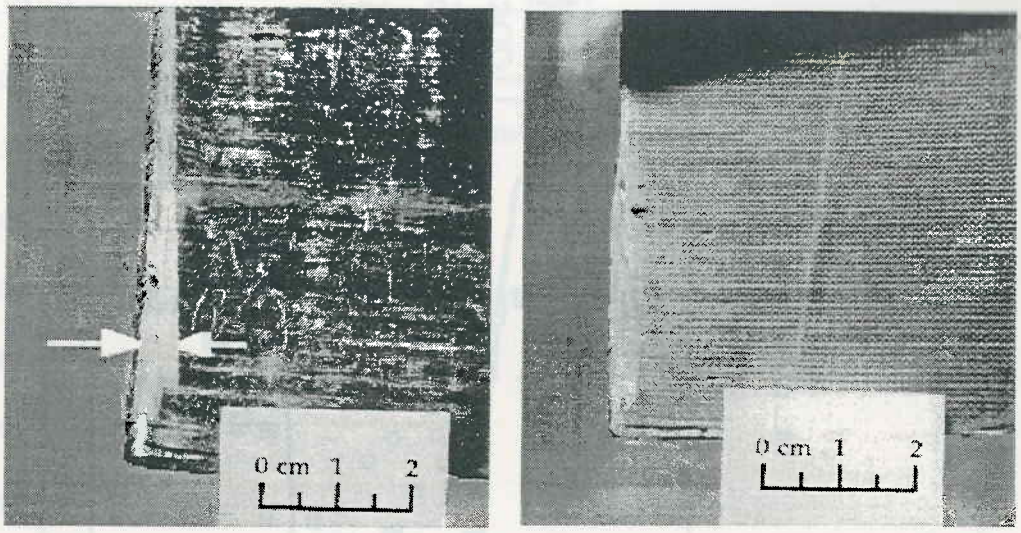

(a) (b)

Figure 25 Comparison of the interply shear occurring at the edge of (a) a (0/90/+45) and (b) a (0/90) c-channel.

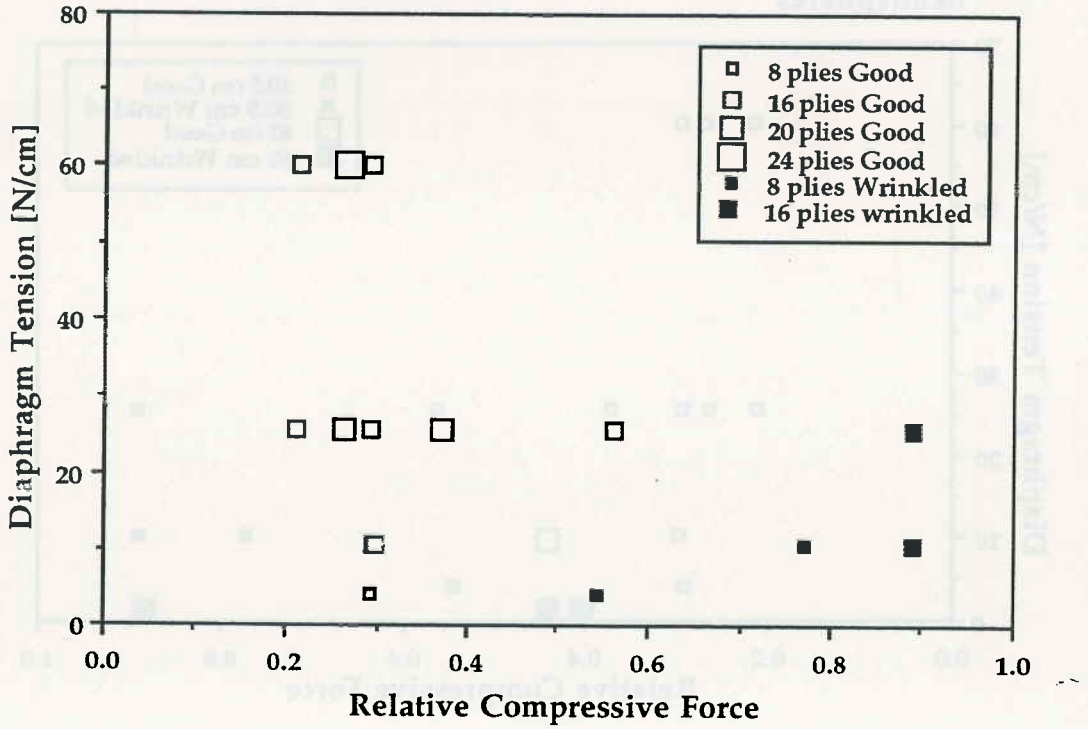

Figure 26 Forming limit diagram for (0/90/+45) 30.5 cm long c-channels.

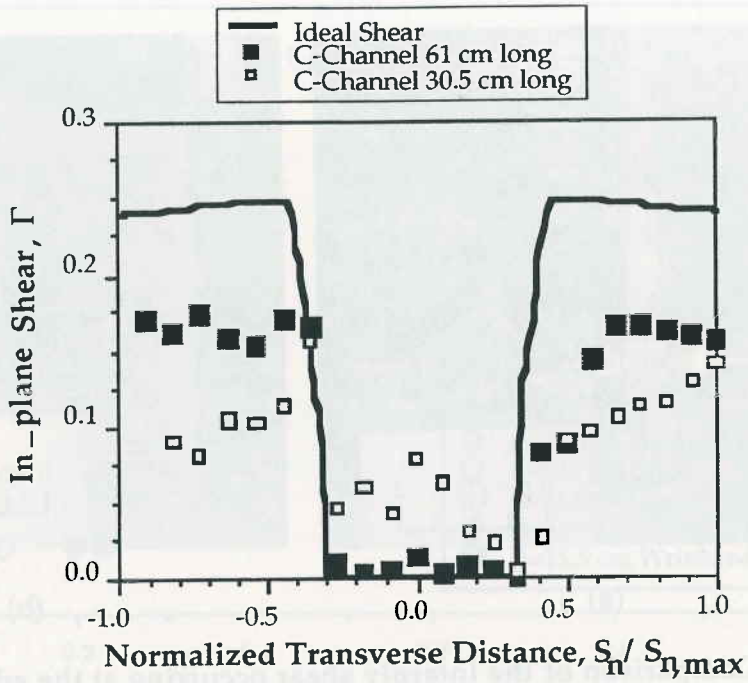

Figure 27 Comparison of ideal fiber and actual fiber shears for c-channels and hemispheres

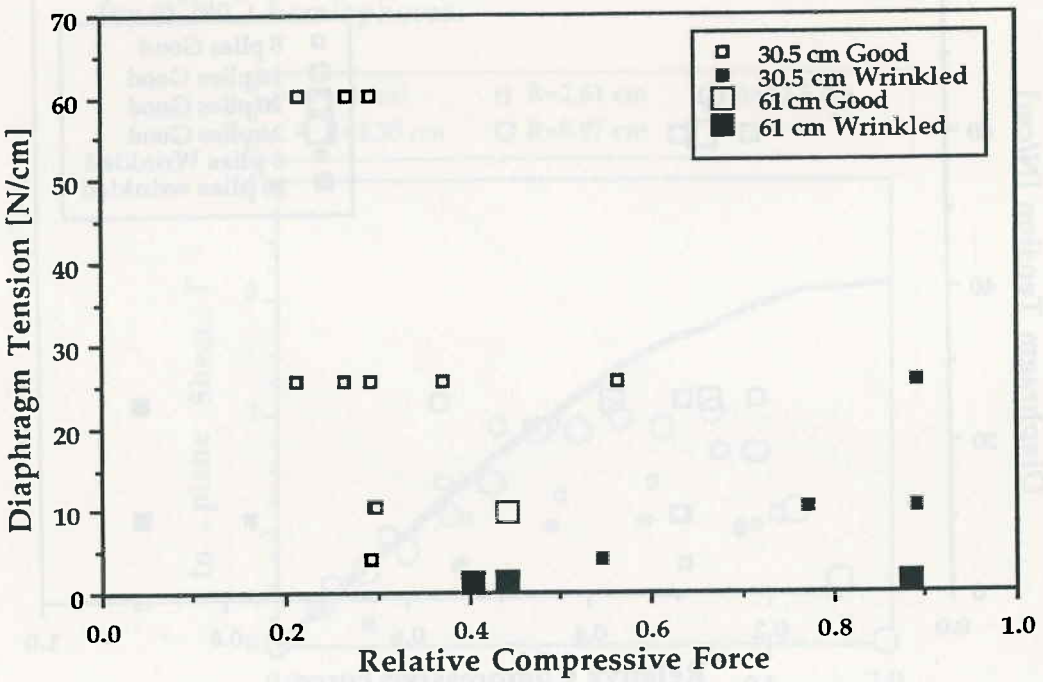

Figure 28 Forming limit diagram for c-channels of two different sizes, plotted using the empirical length scale correction given in Equation 44.

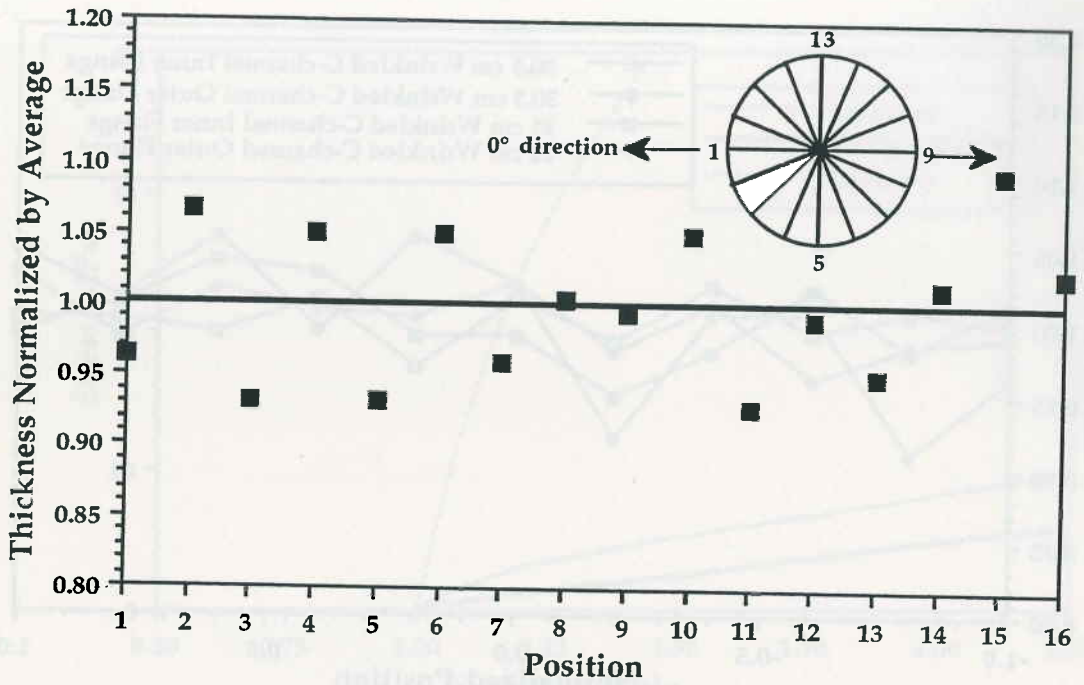

Figure 29 Thickness variation measured around the base of a 0/90 hemisphere.

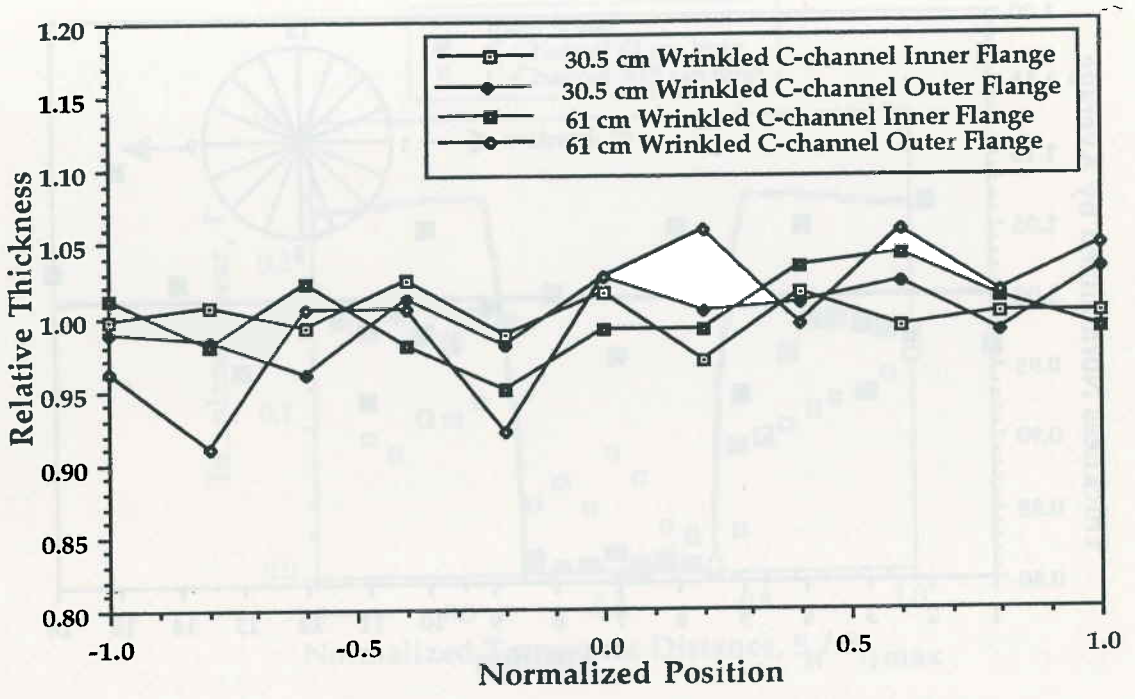

(a)

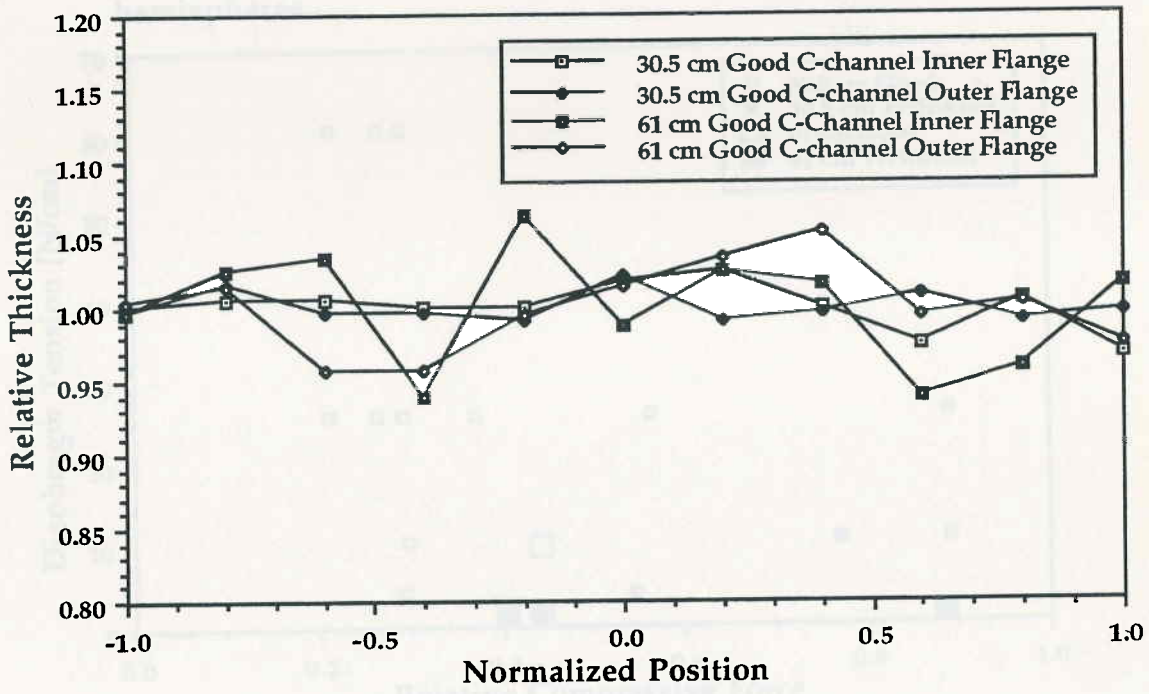

(b)

Figure 30 Thickness variation measured around the base of two different size (0/90±45) c-channels; (a) wrinkled parts and (b) parts formed without wrinkles.

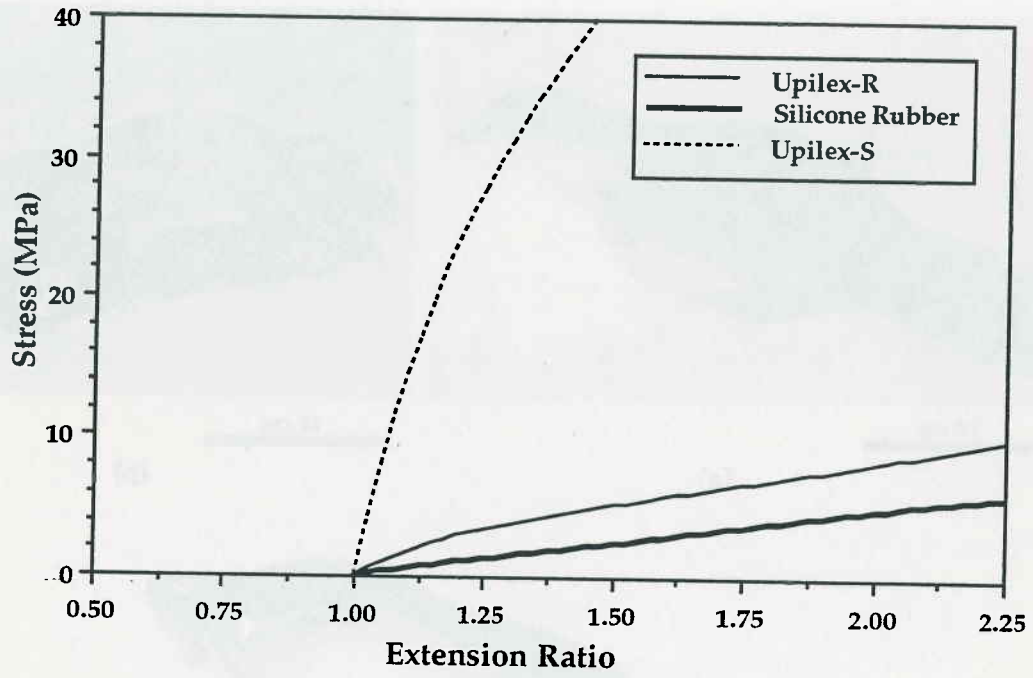

Figure 31 Comparison of biaxial stress curves for diaphragms used with thermoplastic matrix composites (Upilex-R and Upilex S) and the silicone rubber used with thermosets.

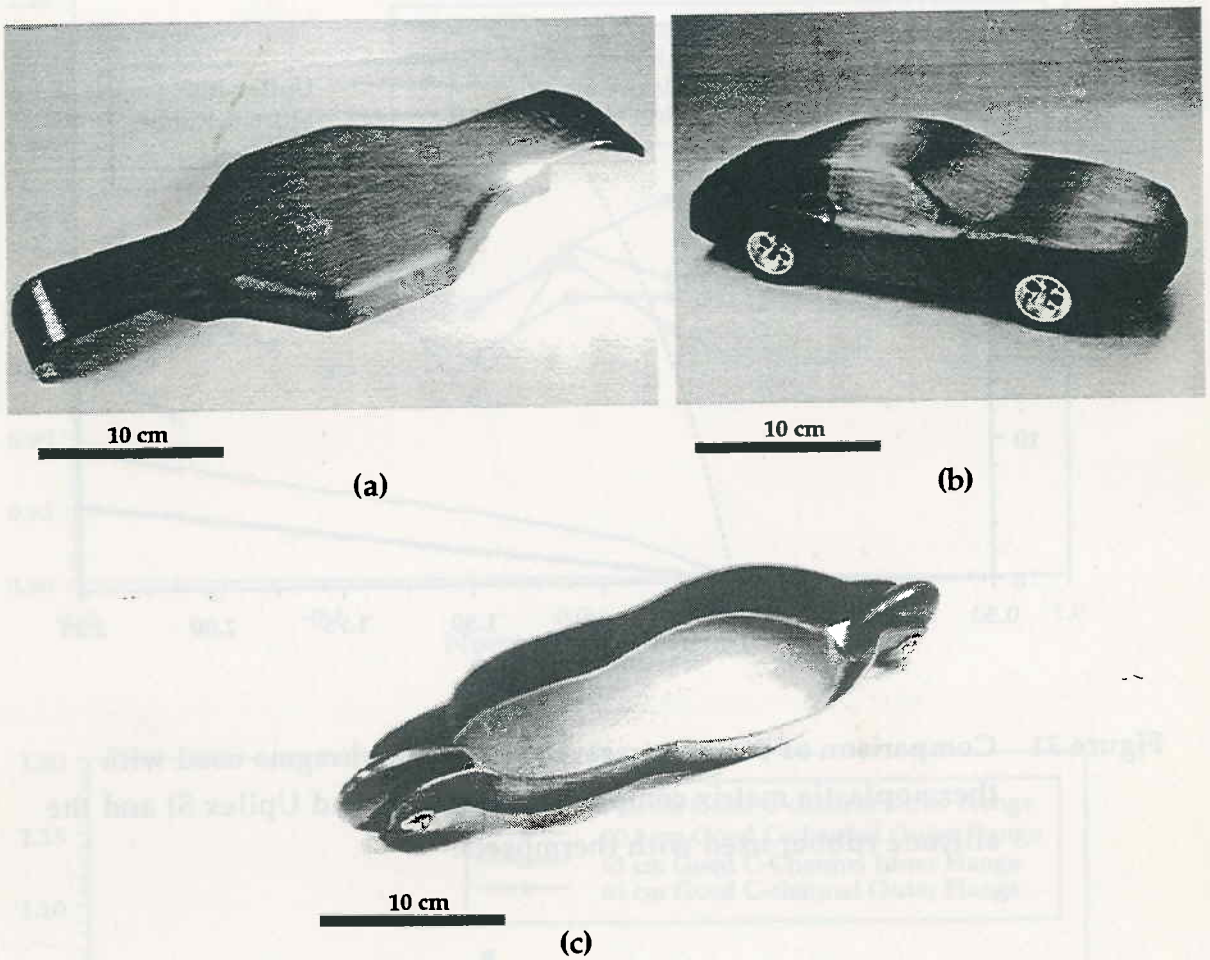

Figure 32 Thermoset matrix parts made by the diaphragm forming process; (a) chassis for a radio controlled model car, (b) scale model automotive body and (c) roller blade.